TEM investigation of reduced activation ferritic/martensitic alloys developed by thermodynamic modeling

O. Kachko [a,*], A. Puype [b], D. Terentyev [c], M. Duerrschnabel [d], M. Klimenkov [d], R.H. Petrov [a]

[a] UGENT, Technologiepark Zwijnaarde 46, Zwijnaarde 9052, Belgium
[b] OCAS NV, Pres. J.F. Kennedylaan 3, Zelzate 9060, Belgium
[c] Belgian Nuclear Research Centre, SCK CEN, Mol 2400, Belgium
[d] Karlsruhe Institute of Technology, Institute for Applied Materials, Eggenstein-Leopoldshafen 76344, Germany

A B S T R A C T

Two reduced activation ferritic/martensitic (RAFM) alloys with chemical compositions guided by thermodynamic modelling were designed, fabricated, and mechanically tested in previous work. The experimental alloys demonstrated significantly refined grain and subgrain size with a high density of dislocations leading to higher yield and tensile strength with respect to EUROFER97–2 without sacrificing the impact toughness. This improvement has been achieved thanks to the dedicated chemical and thermal treatment that alternates the nucleation, growth and coarsening as well as enables the presence of high-density small precipitates as compared to EUROFER97 steel. In this work, TEM investigation was performed to quantitatively describe the microstructural parameters such as the average sizes of $M_{23}C_6$ and MX particles, number density of the particles and dislocation density. Furthermore, the strengthening contribution of each microstructural feature was calculated, and the correspondence of the total strength derived via microstructure to the measured yield strength is discussed.

1. Introduction

Advanced steels for helium cooled design concepts of future DEMO reactor, which allow higher thermal efficiency of the fusion power plants, should be able to operate at temperatures up to 650 °C [1]. Structural material development as part of advance steels WPMAT project (for low and high temperature applications) is focused on two main optimization routes such as alternating thermomechanical treatments and/or optimizing chemical composition of the material to achieve the refinement of grains/subgrains and increased volume fraction of MX carbonitrides [2]. It has been shown in multiple studies that nano-sized MX precipitates formed during thermo-mechanical treatment (TMT) are contributing to high-temperature creep strength by pinning the grain boundaries and dislocations thus stabilizing the martensitic microstructure [3].

Two RAFM alloys for high temperature applications were developed based on thermodynamic modelling in previous work [4]. The chemical composition with increased Ta, V content (model alloy 1) and Ta, N content (model alloy 2) resulted in a high calculated volume fraction of MX precipitates. Reduced C content resulted in low calculated volume fraction of $M_{23}C_6$ precipitates, which tend to coarsen during prolonged ageing at elevated temperatures [5]. The heat treatment that came out of the model was further optimized in a high-throughput mode. Mechanical and microstructural characterization proved the increased high temperature strength of the model alloys and refined grain size compared to the reference material, EU97–2. In this work a TEM investigation was performed with a focus on the characterization of morphology and density of precipitates. High resolution TEM (HR TEM) was used to visualize the martensitic microstructure consisting of high density of dislocations and lath subgrains.

* Corresponding author.
E-mail address: olga.kachko@sckcen.be (O. Kachko).

Table 1
Chemical compositions in wt% and heat treatment of model alloys and EU97–2 [7].

Alloy	C	Mn	Cr	V	W	Ta	N	Si	Ti	Fe	Austenitization	Tempering
MA 1	0.044	0.409	9.032	0.361	0.467	0.488	0.024	–	–	Bal.	1050 °C/30 min	740 °C/50 min
MA 2	0.046	0.406	8.611	0.226	0.853	0.379	0.062	–	–	Bal.	1050 °C/30 min	720 °C/90 min
CNA 2	0.1	0.5	8.6	0.2	1.3	0.1	0.003	0.1	0.01	Bal.	1120 °C/20 min	750 °C/30 min
EU97–2	0.11	0.55	8.95	0.2	1.10	0.12	0.022	0.04	–	Bal.	980 °C/30 min	760 °C/90 min

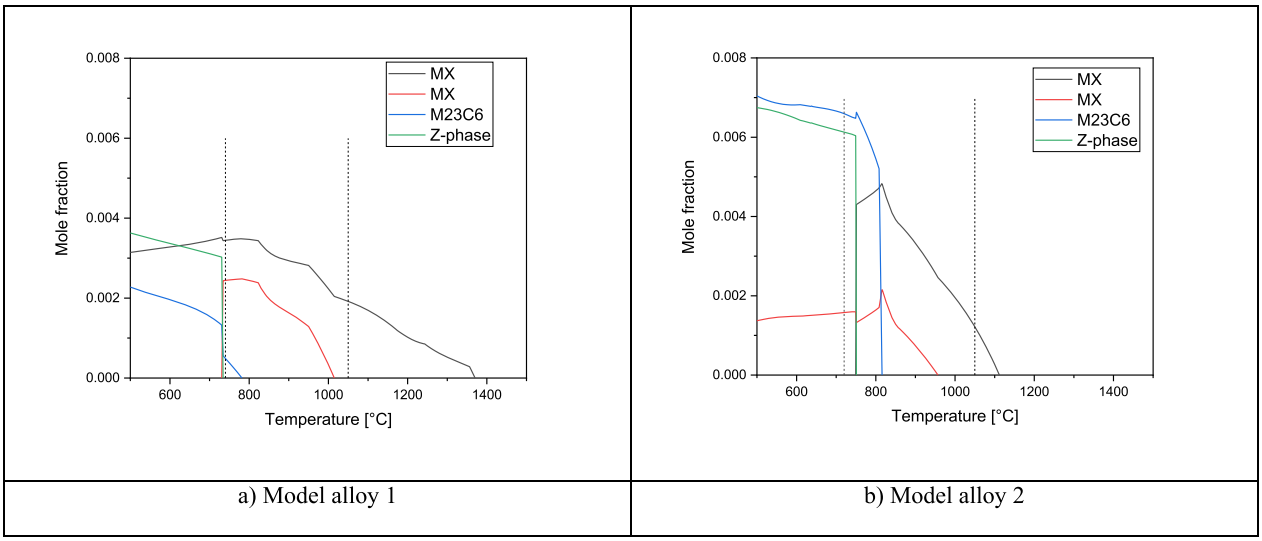

Fig. 1. Temperature evolution of the phase mole fraction in the model alloy 1 (part (a)) and model alloy 2 (part (b)) calculated by Thermocalc. The dotted lines indicate the tempering and austenitization temperature.

2. Materials and methods

TEM analyses were performed in a Thermofisher Talos F200X (scanning) transmission electron microscope, equipped with a Super-X detector for energy dispersive X-ray spectroscopy (EDS), a Gatan Enfinium spectrometer for electron energy-loss spectrometry (EELS) and a Scanning Device (STEM) including a high angle annular dark-field ring detector (HAADF). The microscope was operated at 200 kV accelerating voltage with a field emission gun.

TEM discs of 3 mm diameter were mechanically grinded to the thickness of 0.1 mm. Electrochemical thinning was performed in a Tenupol-3 jet polisher with a 20% H_2SO_4 + 80% CH_3OH solution as electrolyte at a voltage of 10 V at room temperature.

In order to visualize $M_{23}C_6$ precipitates, three 8.825 µm x 8.825 µm sized elemental maps with 8.6 nm pixel size were taken. For the MX-type precipitates, the map sizes were reduced to 3.12 µm x 3.12 µm and pixel size of 3 nm was used to improve the lateral resolution. Particle sizes were evaluated using ImageJ software. Feret's diameter was used as a measure of the precipitate sizes.

3. Results

3.1. Material and heat treatment

Two RAFM alloys with chemical compositions guided by thermodynamic modelling were produced by OCAS NV in a vacuum induction furnace. More details on production route and modelling part can be found in [4]. Model alloy 1 (MA 1) and model alloys (MA 2) have reduced content of C (0.05 wt%) and increased content of Ta (~0.5 wt% Ta for MA 1 and ~ 0.4 wt% Ta for MA 2) as compared to EU97–2. Additionally, MA 1 has an increased V content (~0.4 wt%) and reduced W content (~0.4 wt%). MA 2 has three times more N compared to MA 1, i.e. 0.06 wt% and 0.02 wt%, respectively. Table 1 summarizes the chemical compositions and heat treatments of the model alloys, CNA 2 RAFM steel [6] and the reference material, EU97–2.

Table 2
Volume percent of main phases present at 740 °C (MA 1) and 720 °C (MA 2) calculated with Thermocalc. CNA 2 and EU97–2 are given for comparison.

Alloy	T_eq °C	$M_{23}C_6$ ol%	MX vol%
MA 1	760	0.03	0.59
MA 2	760	0.64	0.57
CNA 2 [6]	760	0.95	0.42
EU97–2 [6]	760	2	<0.2

Thermocalc calculations were performed at the temperatures used in the tempering step of the heat treatment i.e., 740 °C and 720 °C for MA 1 and MA 2 respectively. Computational alloy thermodynamics calculations were conducted with Thermocalc software. The calculated temperature-dependant phase mole fractions present in model alloys are shown in Fig. 1. The dotted line indicates the tempering temperature. It should be noted that there are two types of MX phase at tempering temperatures i.e., MX phase which contains mainly Ta and C and another MX phase which consists of mostly of V and N. However, at austenitization temperature of 1050 °C only one MX phase is present which contains mainly V and N. The phases such as ferrite, austenite and liquid are not included in the plot. Volume percent of each phase present at the equilibrium temperature of 760 °C is shown in Table 2. EU97–2 and CNA 2 were added for a comparison. Calculations resulted in an increased volume percent of MX precipitates and decreased vol% of $M_{23}C_6$ particles compared to EU97–2 and CNA 2. MA 2 and CNA 2 alloys contain a lower vol% of $M_{23}C_6$ compared to EU97–2 whereas MA 1 has even lower vol% of complex carbonitride particles due to reduced W content. MA 1 and MA 2 alloys contain a similar vol% of MX particles i.e., 0.59 and 0.57 vol% respectively, whereas lower amount of MX (0.42 vol%) was reported for CNA 2.

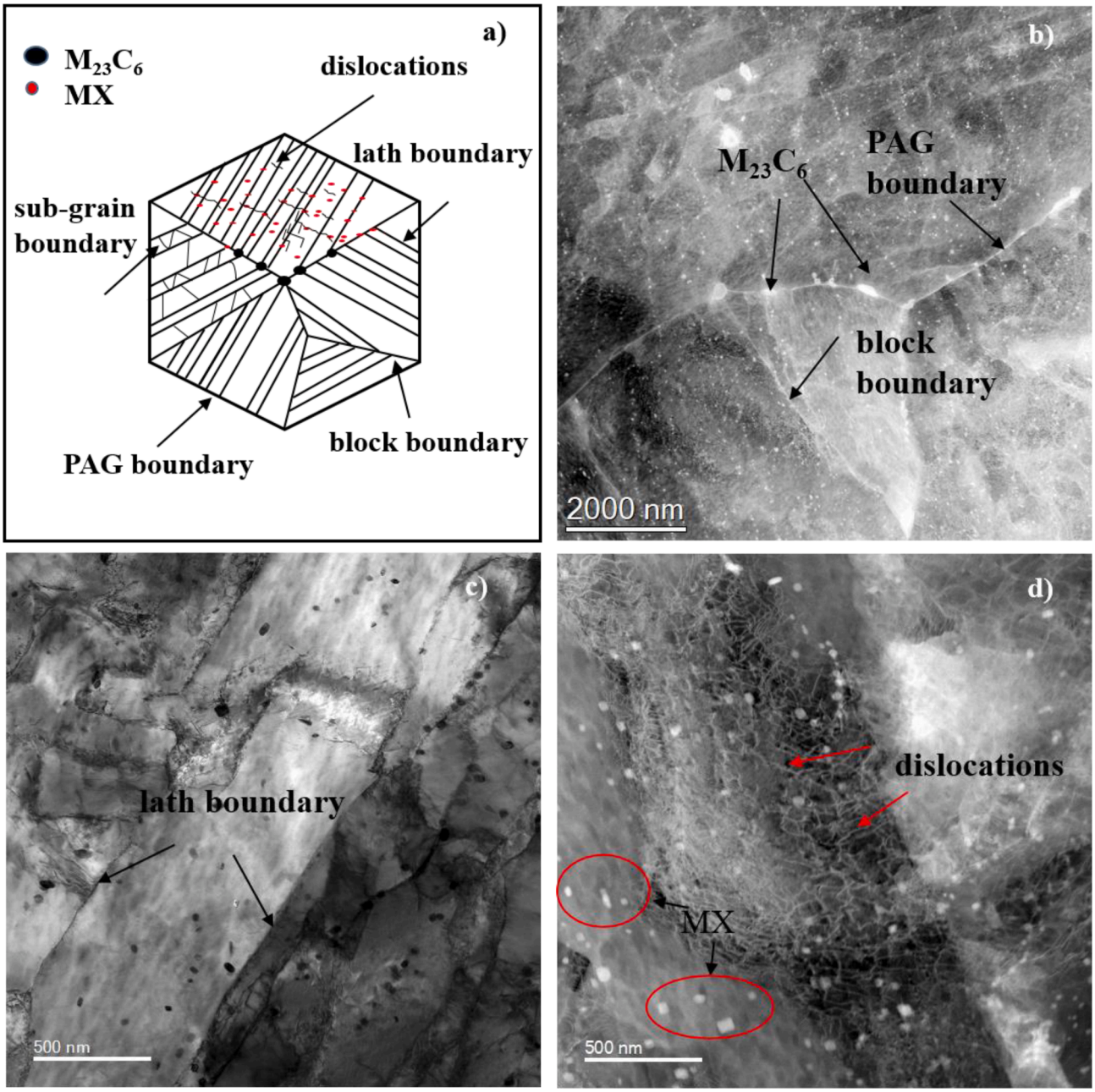

Fig. 2. Microstructure of model alloys. Schematic representation of the microstructure is shown in part (a). STEM images revealing the tempered martensitic microstructure of model alloys are shown in (b) through (d).

3.2. *Microstructural characterization*

The microstructures of both model alloys are shown in Fig. 2. The microstructure of martensitic steels consists of prior austenitic grains (PAGs), blocks and lath grains [8]. From TEM images it can be observed that lath grains are further divided into nanosized subgrains.

Both model alloys exhibit tempered martensitic microstructure with elongated lath grains ranging from 100 nm to 500 nm in width and high dislocation density in the range of 10^{14} m ^{2} after dedicated heat treatments. Very fine precipitates nucleated at dislocations within the subgrains and on the lath boundaries were also observed in both steels. The dislocation density was calculated from TEM images taken at four different areas. The average dislocation density of 1.5×10^{14} m ^{2} was measured for MA 1 and slightly higher density of 2×10^{14} m ^{2} was measured for MA 2. The similar values were also measured for EUROFER97 and EUROFER-ODS alloy in [9]. Typically, the dislocations of ½<111> type are present in the bcc steels.

The thickness of the sample was measured using standard EELS log-ratio technique described in [10]. The modern microscopes allow absolute thickness determination with an accuracy of + / 15%. Since the thickness variations are common in electrochemically etched steel specimens, the average thickness value of region of interest (ROI) was used for the density calculations.

It can be concluded that the dislocation density of the model alloys is very high due to thermomechanical processing such as reheating the plates at 1250 °C for 2 h followed by hot rolling in 6 passes at 1200 °C till 850 °C and subsequent water quenching. In some cases, dislocation junctions were observed which is common in highly deformed materials. Fig. 3 shows the dislocation structure of the model alloys.

There are two types of precipitates present in both model alloys, i.e. coarse Cr-rich $M_{23}C_6$, finer carbo-nitrides rich in Ta and/or V of MX type. Additionally, there were fine nitrides consisting of CrVN, Z-phase,

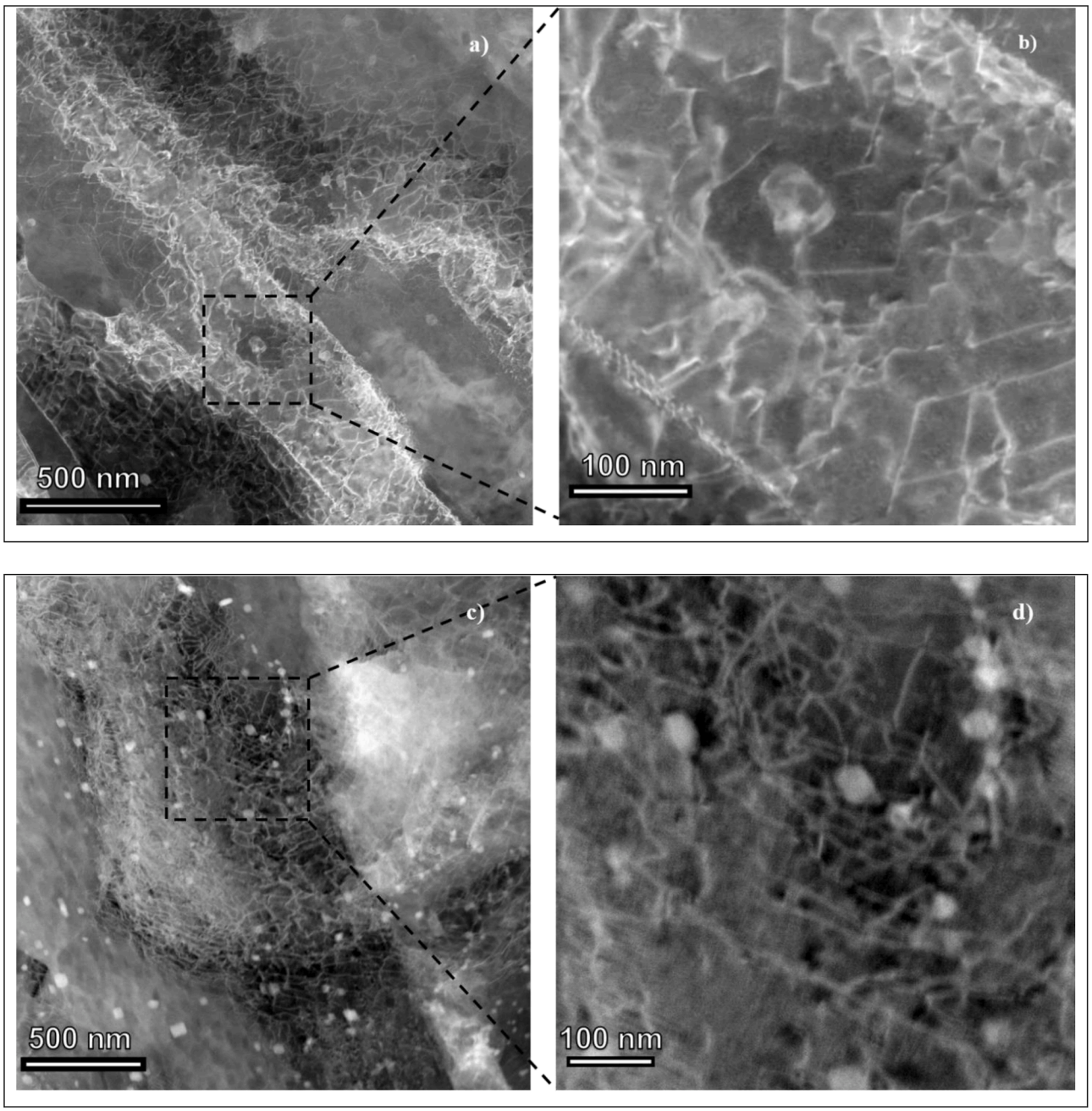

Fig. 3. STEM HAADF images revealing the dislocation structure of model alloys. MA 1 is shown in (a) and in (b) and MA 2 is shown in (c) and (d).

present in model alloy 1. The structure and morphology of precipitates were visualized in HAADF-STEM mode and can be seen in Figs. 4a–7a. The elemental composition maps (see Figs. 4b–i to 7b-i) obtained with the help of EDX show the distribution of elements across the scanned area. Generally, the coarse particles rich in Cr are nucleated at the grain boundaries, often together with V-rich and/or Ta-rich MX particles while very fine MX particles can be observed within the lath and subgrains.

Fig. 8a and 8b show particle size in terms of Feret's diameter of model alloys. Log-normal particle size distributions are shown in Fig. 8c (MA 1) and Fig. 8d (MA 2). Average particle sizes of Cr-rich carbides are 101 nm and 293 nm for MA 1 and MA 2, respectively (see also Table 3). However, there are some large $M_{23}C_6$ particles (>500 nm) present in both alloys. Evaluation of the Ta-rich particle distribution yields average particle sizes of 38 nm for MA 1 and 28 nm for MA 2. V-rich particles have slightly smaller average sizes of 35 nm and 17 nm for MA 1 and MA 2, respectively. The CrVN phase observed in MA 1 has an average size of 32 nm. The presence of Z-phase is consistent with Thermocalc calculations, which predict the dissolution of this phase around 730 °C, close to tempering temperature of MA 1. Z-phase was also predicted by Thermocalc for MA 2 around tempering temperature of 720 °C. Nevertheless, it was not observed experimentally.

3.3. *Strengthening contributions*

An estimation of the strengthening mechanisms, based on the back-stress concept described in [11], was made taking into account individual contributions of microstructural features such as grain boundaries, dislocations and precipitates. Contribution from the free dislocations (so-called "forest hardening") was estimated based on the following equation [8]:

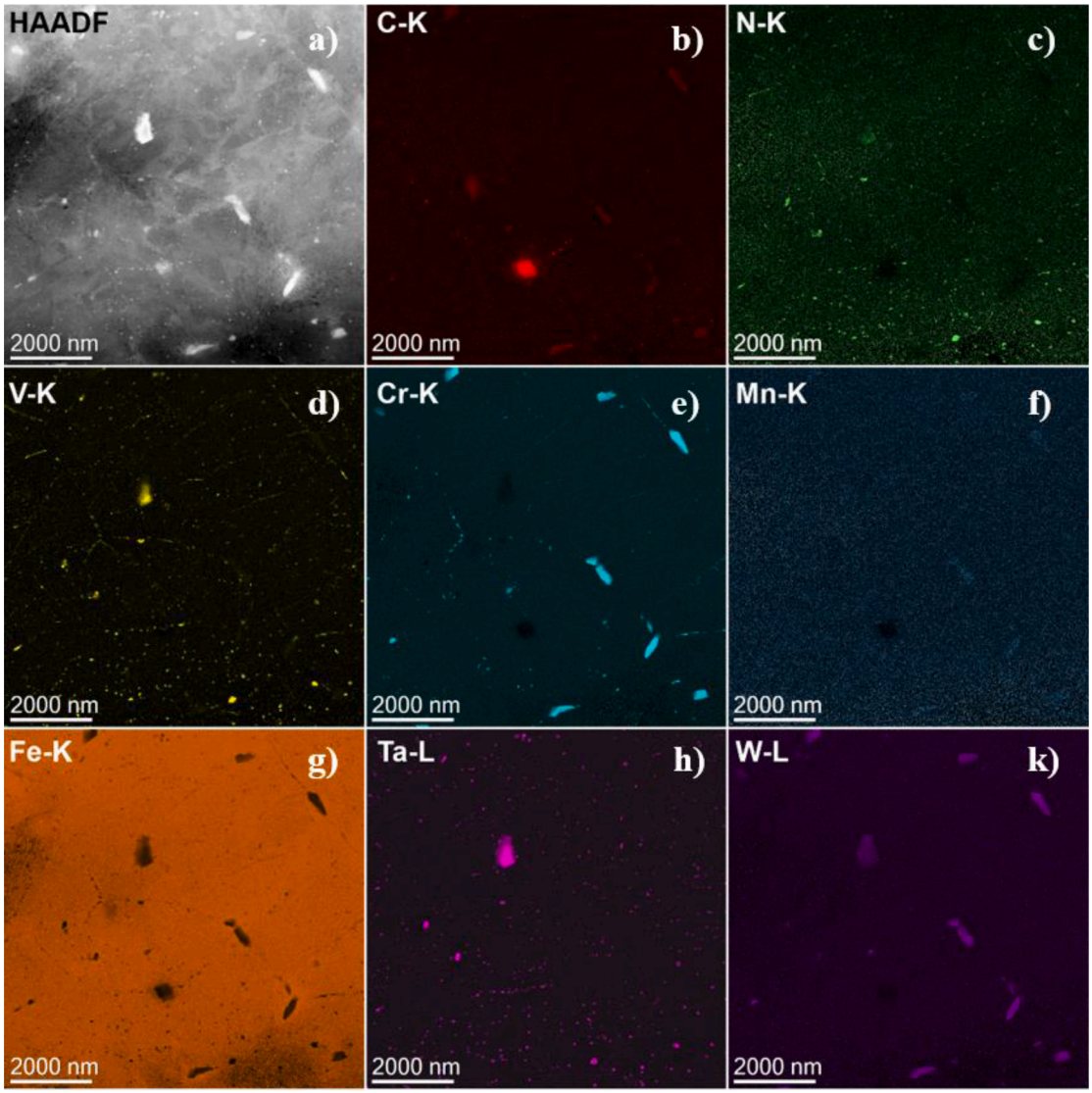

Fig. 4. HAADF image in (a) and elemental maps in (b) through (k) obtained using corresponding EDX line of MA 1.

$$\Delta\sigma_d \approx 0.5\mathrm{MGb}\sqrt{\rho} \quad (1)$$

where b is the length of the Burgers vector, G is the shear modulus and M is the Taylor factor. Taylor factor is equal to 2.9 for ferritic steels [12] and shear modulus is 80.8 GPa at 25 °C. Burgers vector is 0.25 nm for most common dislocations in BCC structure with $b = a_0/2<111>$ where a_0 is the lattice parameter. Strengthening due to prior austenite grain boundaries was evaluated as:

$$\Delta\sigma_g \approx \beta\mathrm{MGb}/\sqrt{d_g} \quad (2)$$

where β is a strengthening constant equal 4380 $m^{1/2}$ [13] and d_g is grain size. Contribution from lath boundaries and precipitate strengthening was estimated with the help of Orowan stress equation [14]. Lath contribution to the strength of the material is given by:

$$\Delta\sigma_l \approx \frac{MGb}{\lambda} \quad (3)$$

where λ is the lath width and precipitate strengthening is given by the dispersed barrier model [15]:

$$\Delta\sigma_p \approx \alpha\mathrm{MGb}\sqrt{Nd_p} \quad (4)$$

where α is a strength factor and for spherical precipitates is given as [16]:

$$a = \frac{0.135}{(\sqrt{1-\nu})(1-0.816d_p\sqrt{Nd_p})}\ln\left(\frac{0.816d_p}{r_o}\right) \quad (5)$$

Strength factor ranges from 0.6 to 1 depending on the particle sizes, N is the number density of the precipitates and d_p is the particle diameter. Experimentally determined parameters include number density N, dislocation density ρ, particle diameter d_p, grain size d_g and lath width λ. Table 4 summarizes the parameters used in the above equations. The subscripts in the terms in the equations denote contributions from dislocations (d), precipitates (p), grain boundaries (g) and lath structure (l).

Table 5 includes the calculated strength contributions, i.e. σ_g, σ_l, σ_p and σ_d, to the total strength of the model alloys at room temperature. The greatest contribution to the strength of the materials is attributed to the dislocations and lath boundaries. Particle strengthening was divided into three contributions according to the type of particle considered. MX particles were split into V-rich and Ta-rich carbonitrides. The minimum strength was calculated by using the lath thickness of 500 nm and lowest dislocation density of $4*10^{13}$ m^{-2}. For the maximum strength, a lath thickness of 100 nm and highest dislocation density of $3*10^{14}$ m^{-2} was used.

Examining the individual contributions of the different mechanisms

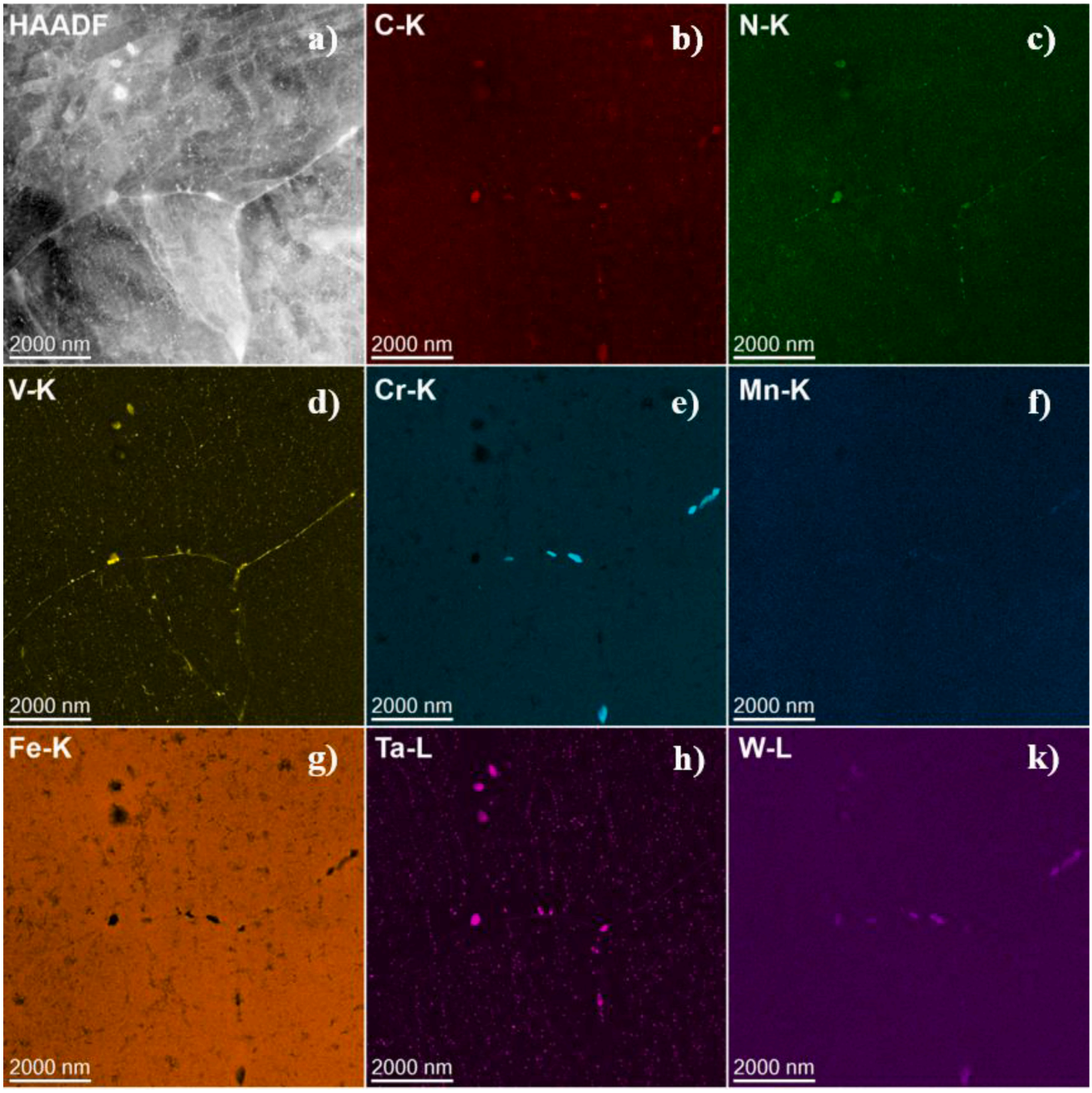

Fig. 5. HAADF image in (a) and elemental maps in (b) through (k) obtained using corresponding EDX line of MA 2.

to the total back-stress, it should be noted that linear superposition rule cannot be applied to calculate the total contribution of all types of precipitates and other lattice defects (i.e., dislocations, lath boundaries, etc.) because different types of defects represent different resistance against plastic slip. Hence, the linear superposition rule would lead to the overestimation of the total strength. For this reason, different rules, shown in Table 6, were used to demonstrate different approaches in calculating the strength of the model alloys based on the combination of linear and root-sum-square laws. The first estimation (see Eq. (6)) is given by using a linear law and considering only the particles with the greatest strength contribution, namely TaC. The other three equations are based on applying root-sum-square law to different types of obstacles such as lath and dislocations (Eq. (7)), different types of precipitates (Eq. (8)) and precipitates and dislocations (Eq. (9)).

The term σ_i indicates the strengthening contribution of all types of precipitates added up. Relative error was calculated as a ratio of the total calculated strength and the measured yield strength. Applying Eq. 6 to Eq. 8 gave a relative error between 6 and 18% whereas the error of $\leq$5% was calculated by using Eq. (9). Eq. (9) is considered in this work as the most consistent with the approach described in [17,18]. In Eq. (9) the root-sum-square law was applied to calculate the contribution to the strength from all type of particles and dislocations, which have similar strength factor of 0.5–0.6 and act on the scale of several nanometres, combined with a linear law for PAG and lath boundaries, which have a similar strength factor of 1 but very different length scale and dissimilar strength contributions.

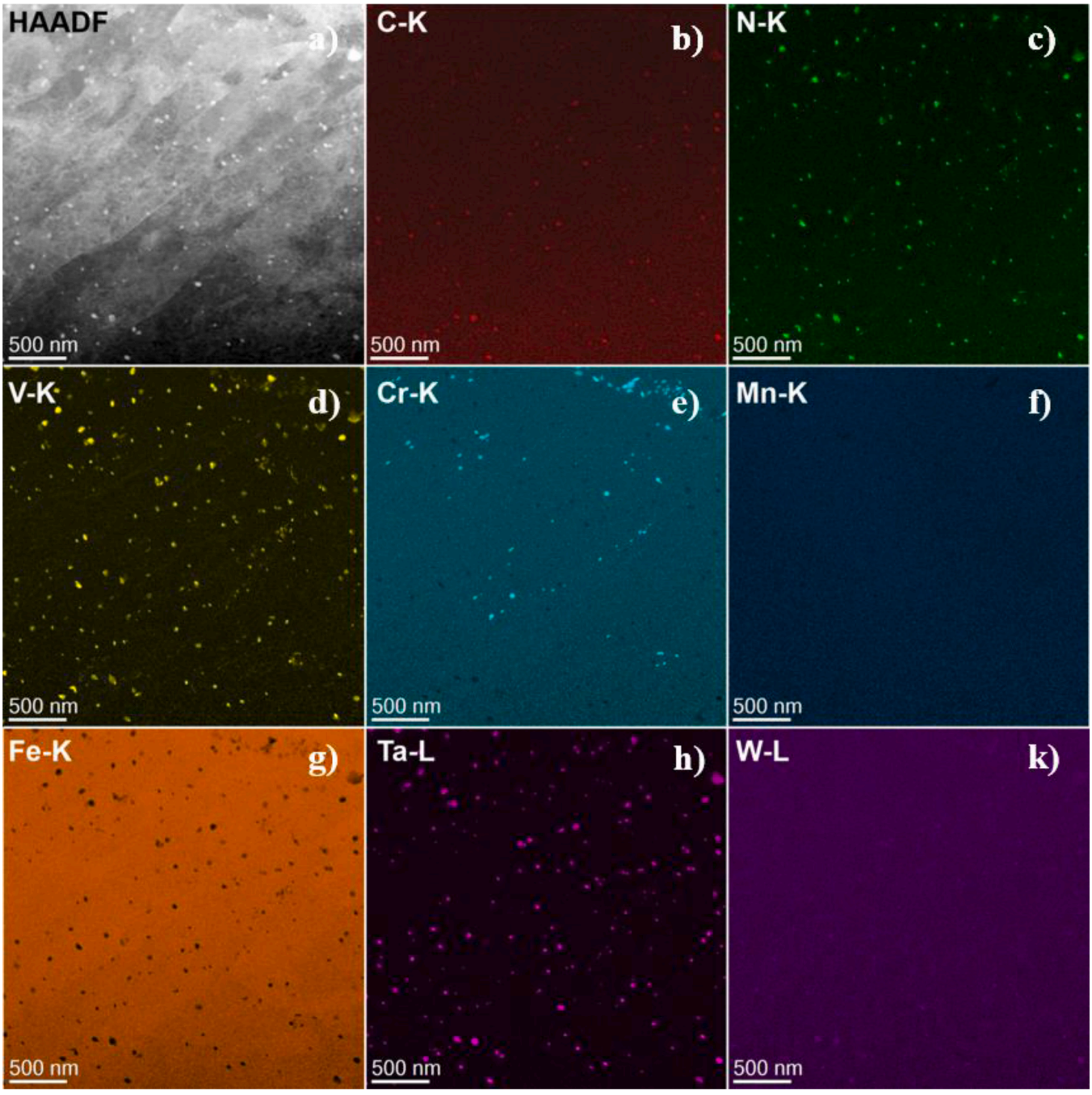

Fig. 6. HAADF image in (a) and elemental maps in (b) through (k) obtained using corresponding EDX line of MA 1.

4. Discussion

Model alloys investigated in this work, were designed to extend the upper operational temperature limit, thus, to have improved creep resistance compared to EUROFER97. It can be concluded from the literature that in order to improve the creep strength of 9%Cr ferritic/martensitic steels without compromising the low temperature ductility, a fine lath structure with a high density of free dislocations within the subgrains is required [19]. However, high dislocation density stores elastic energy, which acts as a driving force for recovery of the material exposed to stresses at elevated temperatures. To suppress the dislocation recovery and to pin the lath/subgrain boundaries movement, a high volume of finely dispersed MX particles is required [20].

Model alloys, with a chemical composition guided by thermodynamic modelling, showed a fine lath/subgrain martensitic structure (100–500 nm) with a high dislocation density in the order of 10^{14} m ^{2}.

Additionally, model alloys have a greater volumetric fraction of MX precipitates compared to other RAFM steels (see Table 7) as predicted by Thermocalc and determined experimentally. Higher yield strength of MA 2 as compared to MA 1 is attributed to a higher number density of finer MX precipitates concentrated on the grain/subgrain boundaries and slightly higher dislocation density. The measured vol% of MX particles in both alloys is greater than expected from the thermodynamic calculations. The difference could arise from the fact that MX particles were considered as Ta-rich and V-rich MX separately in post-processing analysis of elemental maps. It could lead to an overestimation of the number density of MX particles and thus a greater measured volume

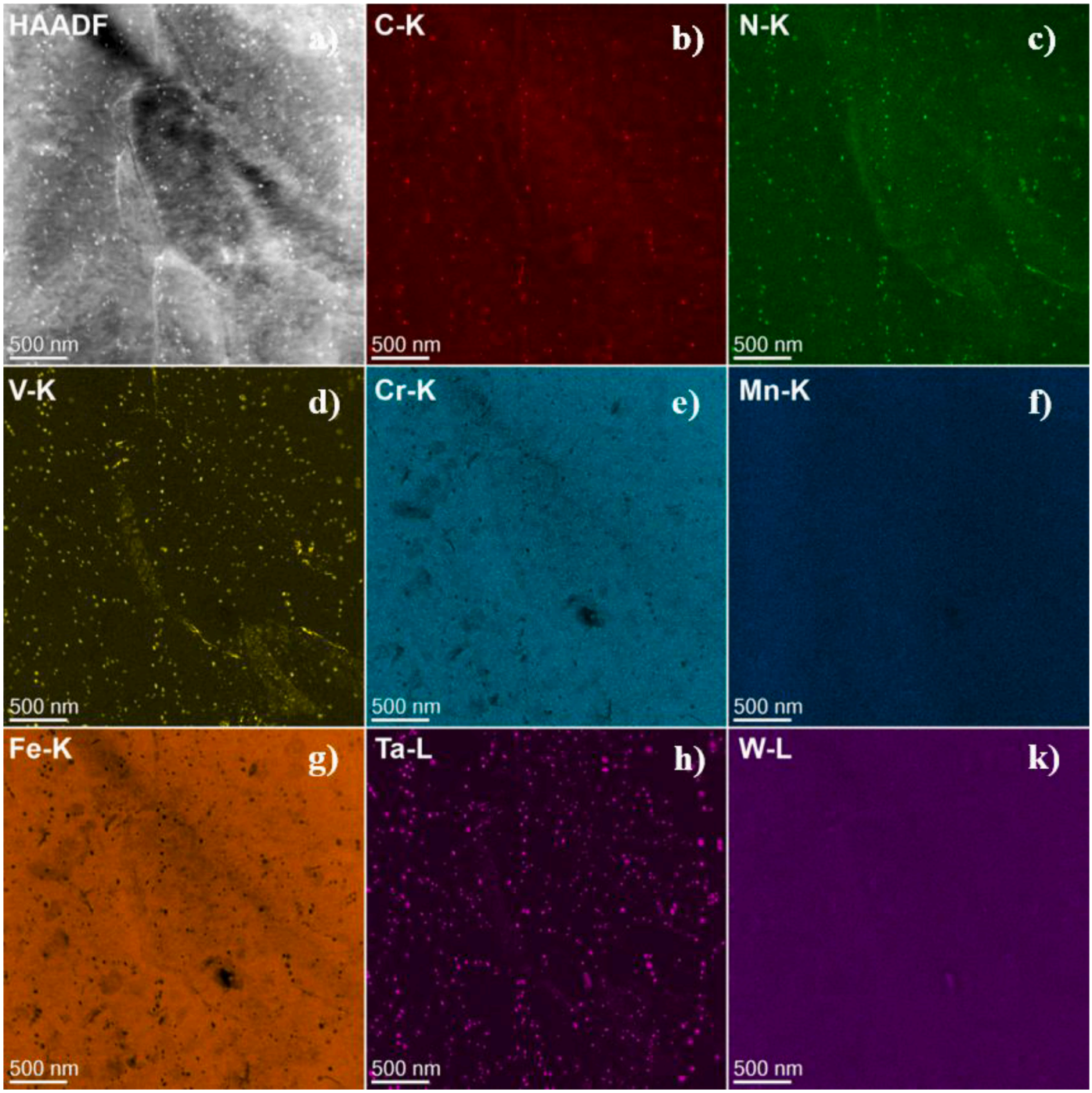

Fig. 7. HAADF image in (a) and elemental maps in (b) through (k) obtained using corresponding EDX line of MA 2.

fraction. Regarding $M_{23}C_6$, the vol% is very similar in two model alloys and is in a good agreement with the Thermocalc calculations for MA 2. However, there was a major discrepancy for MA 1. About 20 times greater amount of $M_{23}C_6$, 0.73 vol%, was observed experimentally compared to 0.03 vol% predicted by Thermocalc. The lower calculated vol% of $M_{23}C_6$ in MA 1 as compared to MA 2 was also observed at equilibrium temperature of 700 °C in the previous study [4]. Such a low volume fraction could be explained by reduced C content in combination with reduced W content because less W is available to form complex (Cr, W) carbides. However, since both model alloys have the same amount of C (0.045 wt%) and the same vol% of $M_{23}C_6$ as determined by TEM, it can be concluded even though W is necessary for the formation of complex carbides, it is the availability of C that determines the fraction of Cr and W in the precipitates as well as volume fraction of $M_{23}C_6$. Also, it is interesting to note, that although the experimental volume fraction of $M_{23}C_6$ is similar in both alloys, the average size of these particles differs, and it is much greater in MA 2. This could result from the longer tempering time of MA 2 as compared to MA 1, as smaller $M_{23}C_6$ particles have a tendency to coarsening at the constant volume fraction [21].

From the previous work, it is known that tensile properties of the model alloys MA 1 and MA 2 were superior compared to EU97–2 i.e., greater yield and tensile strength up to maximum studied temperature being 600 °C. The increase in the strength of the model alloys is attributed to the increased dislocation density, grain/lath refinement and greater number density of finely dispersed MX precipitatesThe enhanced strength is achieved at the cost of slight reduction of ductility

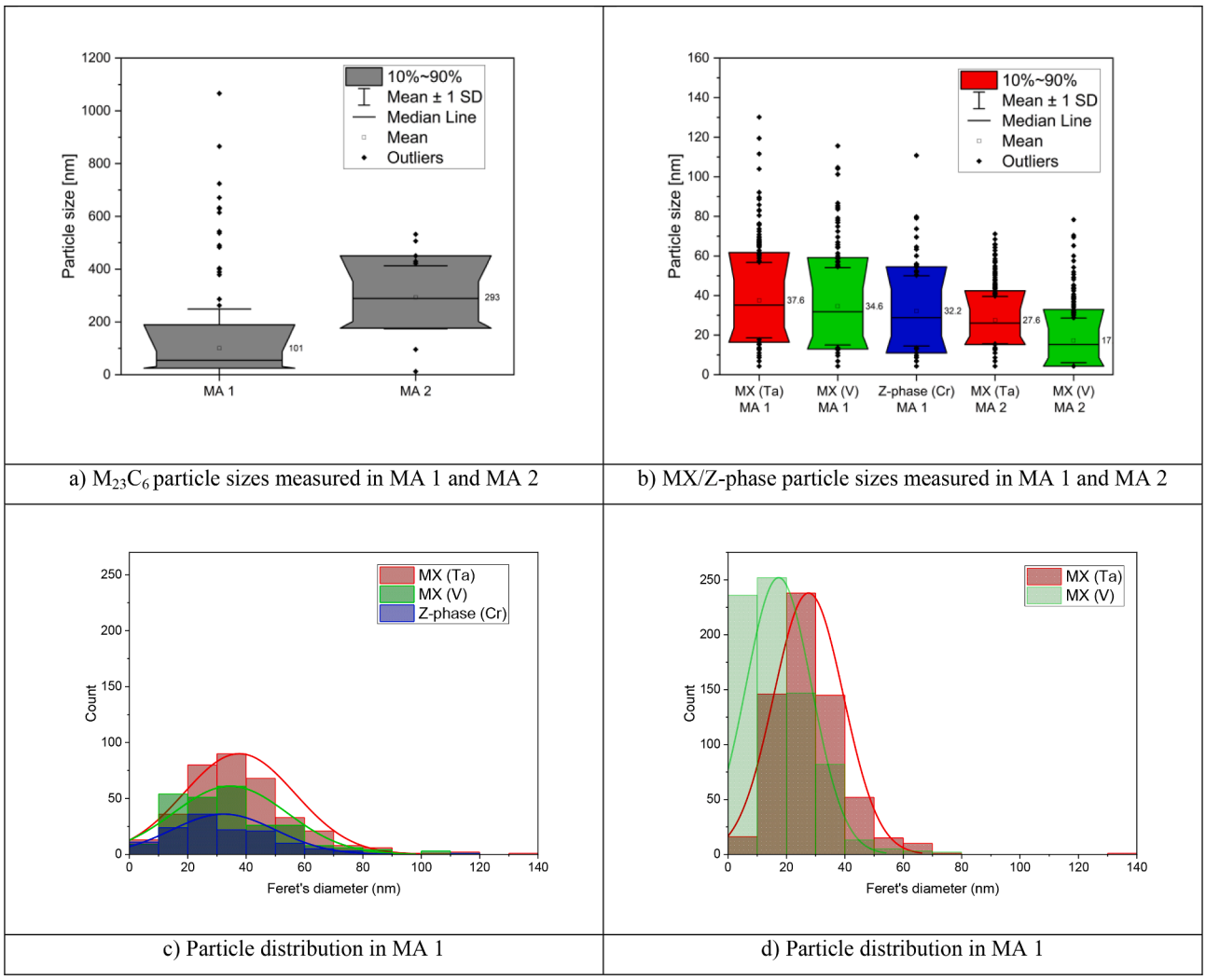

a) $M_{23}C_6$ particle sizes measured in MA 1 and MA 2

b) MX/Z-phase particle sizes measured in MA 1 and MA 2

c) Particle distribution in MA 1

d) Particle distribution in MA 1

Fig. 8. Statistics on the measured particle sizes in (a) M23C6 and in (b) MX and Z-phase. Particle size distribution is shown in (c) and (d) for MA 1 and MA 2, respectively.

Table 3
Microstructural characteristics of model alloys.

Alloy name	Grain size	Lath size	ρ	$M_{23}C_6$		Ta-rich MX		V-rich MX		CrVN	
				d	N	d	N	d	N	d	N
	μm	nm	m^{-2}	nm	m^{-3}	nm	m^{-3}	nm	m^{-3}	nm	m^{-3}
MA 1	14	100–500	1.5×10^{14}	101	1.35×10^{19}	38	1.9×10^{20}	35	1.3×10^{20}	32	7.12×10^{19}
MA 2	11.5	100–500	2×10^{14}	293	5.60×10^{17}	28	4.48×10^{20}	17	5.32×10^{20}	–	–

Table 4
Parameters used in the back-stress strengthening model.

Parameter	Name	Value	Parameter	Name	Value
α	Strength factor	~0.6–1	N	Number density	10^{17}–10^{20} m^{-3}
M	Taylor factor	2.9	d_p	Particle size	17–290 nm
G	Shear modulus	80.8 GPa	d_g	Grain size	12–14 μm
b	Burgers vector	0.25 nm	λ	Lath width	100–500 nm
β	Constant	4380 $m^{-1/2}$	ρ	Dislocation density	10^{13}–10^{14} m^{-2}

for MA 2. Furthermore, model alloys demonstrate good toughness, which is attributed to the refined grain size and increased Ta content. The model alloys showed the Charpy impact toughness comparable to (MA 2) or greater than that of EU97–2, namely a higher USE and lower DBTT (MA 1), thereby demonstrating the required low temperature performance.

Overall, it can be concluded that the desired microstructure aimed to improve the creep strength was achieved for the model alloys, which chemical composition and heat treatment was modified compared to EU97–2, following the guidance of the thermodynamic modelling. It has been shown by several research groups [22–24] that high density of fine MX precipitates result in improved creep strength of 9–12% Cr steels. Others report inhomogeneous growth of MX carbonitrides during creep deformation [25]. Further investigation is needed to systematically

Table 5
Comparison of microstructural features and strengthening contributions at room temperature for 9Cr RAFM steels, 9Cr CNAs, and model alloys.

Parameter	Strengthening by	MA 1				MA 2				CNA 2 [6]	EU97 [6]
		MPa				MPa				MPa	MPa
σ_g	PAGs	68.6				75.8				36	30–80
σ_l	Lath	min		mean	max	min		mean	max	147	120
		117		195	586	117		195	586		
σ_p	$M_{23}C_6$	57				29				81	40–140
σ_p	Ta-rich MX	111				137				358	60–140
σ_p	V-rich MX	89				108					
σ_d	Dislocations	min	mean		max	min	mean		max	507	400
		185	359		507	185	414		507		
σ_{min}		544				569				–	–
σ_{max}		1100				1124				–	–
σ_{mean}		733				807				727	<500
σ_{yield}		655				762				783	~540

Table 6
Estimation of the yield strength of model alloys.

Equation used	MA 1 MPa	Rel. error %	MA 2 MPa	Rel. error %
$\sigma_g + \sigma_l + \sigma_d + \sigma_{TaC} \#(6)$	733	12	822	8
$\sum_i \sigma_i + \sigma_{g+}\sqrt{\sigma_l^2 + \sigma_d^2} \#(7)$	733	12	807	6
$\sigma_g + \sigma_l + \sigma_d + \sqrt{\sum_i \sigma_i^2} \#(8)$	775	18	862	13
$\sigma_g + \sigma_l + \sqrt{\sum_i \sigma_i^2 + \sigma_d^2} \#(9)$	654	0.1	721	5

assess the effect of precipitate evolution on creep behaviour of RAFM steels. Therefore, creep tests on model alloys will be performed in order to finalize the mechanical characterization and make a conclusion about the obtained microstructure and the behaviour of the model alloys at elevated temperatures and constant stresses. Additionally, neutron irradiation studies are launched to validate the stability of the refined laths and dislocation density under higher irradiation temperature and to evaluate the embrittlement induced at low irradiation temperature.

5. Conclusions

The microstructure of new advanced RAFM steels for high temperature applications with a chemical composition guided by thermodynamic modelling has been investigated. The main changes in chemical composition compared to the reference material EUROFER97 were a reduced C content to reduce the volume fraction of coarse $M_{23}C_6$ precipitates and an increased content of Ta and V to promote the formation of fine MX precipitates. The heat treatment of the model alloys has been modified compared to EU97–2. The austenitization temperature was increased to 1050 °C (T_{aust} of EU97–2 is 980 °C) in order to dissolve a greater amount of the primary carbonitrides. The tempering temperature of 740 °C and 720 °C and tempering time of 50 min and 90 min for MA 1 and MA 2, respectively, were chosen as an optimized heat treatment based on the results from the previous study. The main findings of this work are summarized as follows:

- Applied TMT treatment has produced tempered martensitic microstructure with refined prior austenite grains consisting of blocks of several μm and elongated martensite laths ranging from 100 nm to 500 nm with a very high dislocation density in the range of 10^{14} m ^{2} leading to a greater yield and tensile strength of model alloys as compared to EUROFER97.
- Reduction of C content from 0.1 to 0.05 wt% resulted in a decreased amount of $M_{23}C_6$ as calculated by Thermocalc and confirmed experimentally in this work.
- Higher Ta and V content in MA 1 resulted in a greater volume fraction of MX precipitates as compared to MA 2, namely 0.84 vol% and 0.65 vol% for MA 1 and MA 2 respectively. However, the greater number density and finer particle size of MX was observed in MA 2, which implies that the kinetics of the precipitation was different in these two alloys (to be expected given the differences in the applied heat treatment).
- Longer tempering time of 90 min in MA 2 resulted in a lower density of $M_{23}C_6$ precipitates with a greater average size but a smaller spread between lower and upper particle size detected i.e., from ~100 nm to 500 nm with 290 nm on average. However, there was a remarkable spread of particle sizes in MA 1 ranging from ~20 nm to 1000 nm resulting in an average size of 100 nm. The longer tempering time is suggested for MA 1 to completely dissolve Z-phase which might influence the precipitation kinetics of $M_{23}C_6$ carbides.
- The total strengthening calculated by using Eq. (9) from microstructural components in MA 1 and MA 2 is in a good agreement with measured yield strength of the model alloys.
- Overall, the alternation of the microstructure by applying a chemical tailoring followed by the dedicated TMT treatment was proven to be an effective tool to promote the formation of small fine-dispersed MX precipitates as confirmed by the performed microstructural study.

CRediT authorship contribution statement

O. Kachko: Writing – original draft, Writing – review & editing,

Table 7
Volume fraction of precipitates calculated by Thermocalc (TC) and determined experimentally (TEM).

Alloy	T_calc	Heat treatment	MX TC vol%	MX TEM vol%	$M_{23}C_6$ TC vol%	$M_{23}C_6$ TEM vol%	YS MPa	UTS MPa	USE J	e_t %	DBTT °C
MA 1	760 °C	1050C/30′_740C/50′	0.59	0.84	0.03	0.73	655	765	10	26	107*
MA 2	760 °C	1050C/30′_720C/90′	0.57	0.65	0.64	0.74	756	831	9.3	23	96*
CNA 2	760 °C	1120C/20′_750C/30′	0.42	0.36	0.95	–	783	–	–	15	60**
EU97–2	760 °C	980C/30′_760C/90′	0.20	–	2.00	–	537	661	9.7	24.5	90*

* KLST samples.
** half-sized samples.

Investigation, Visualization. **A. Puype:** Conceptualization, Methodology, Formal analysis, Investigation. **D. Terentyev:** Writing – review & editing, Supervision, Funding acquisition. **M. Duerrschnabel:** Writing – review & editing. **M. Klimenkov:** Writing – review & editing. **R.H. Petrov:** Conceptualization, Supervision.

Declaration of Competing Interest

The authors declare that they have no known competing financial interests or personal relationships that could have appeared to influence the work reported in this paper.

Data availability

Data will be made available on request.

Acknowledgements

This work has been carried out within the framework of the EUROfusion Consortium and has received funding from the Euratom research and training program 2014-2018 and 2019-2020 under grant agreement No 633053. The views and opinions expressed herein do not necessarily reflect those of the European Commission. SCK CEN acknowledges the financial support of FOD grant provided for fusion R&D.

References

[1] Romanelli, F., et al., European research roadmap to the realisation of fusion energy. 2018.
[2] G. Pintsuk, et al., Materials for in-vessel components, Fusion Eng. Des. 174 (2022), 112994.
[3] F. Abe, et al., Stabilization of martensitic microstructure in advanced 9Cr steel during creep at high temperature, Mater. Sci. Eng. A 378 (2004) 299–303.
[4] O. Kachko, et al., Development of RAFM steels for high temperature applications guided by thermodynamic modelling, Nucl. Mater. Energy 32 (2022), 101211.
[5] M. Godec, D.A.S. Balantič, Coarsening behaviour of M23C6 carbides in creep-resistant steel exposed to high temperatures, Sci. Rep. 6 (2016), 29734.
[6] L. Tan, L.L. Snead, Y. Katoh, Development of new generation reduced activation ferritic-martensitic steels for advanced fusion reactors, J. Nucl. Mater. 478 (2016) 42–49, 2016.
[7] Materna-Morris, E., Structural Material EUROFER97-2, Characterization of Rod and Plate Material: Structural, Tensile, Charpy and Creep Properties. 2007, Forschungszentrum Karlsruhe.
[8] K. Maruyama, K. Sawada, J.I. Koike, Strengthening mechanisms of creep resistant tempered martensitic steel, ISIJ Int. 41 (6) (2001) 641–653, 2001.
[9] C. Dethloff, E. Gaganidze, J. Aktaa, Review and critical assessment of dislocation loop analyses on EUROFER 97, Nucl. Mater. Energy 15 (2018) 23–26.
[10] T. Malis, S.C. Cheng, R.F. Egerton, EELS log-ratio technique for specimen-thickness measurement in the TEM, J. Electron Microsc. Tech. 8 (2) (1988) 193–200.
[11] E. Kozeschnik, I. Holzer, Precipitation During Heat Treatment and Service: Characterization, Simulation and Strength Contribution, Woodhead publishing in materials, 2008.
[12] U.F. Kocks, The relation between polycrystal deformation and single-crystal deformation, Metall. Trans. 1 (1970) 1121–1143.
[13] C.C. Eiselt, Eigenschaftsoptimierung der Nanoskaligen Ferritischen ODSLegierung 13Cr-1W-0.3Y2O3-0.3TiH2, Metallkundliche Charakterisierung und Bestimmung von Struktur-Eigenschaftskorrelationen, Karlsruhe Karlsruhe Institute of Technology, 2010.
[14] J. Cadek, Creep in Metalic Materials, Institute of Physical Metallurgy of the Czechoslovak Academy of Sciences, 1988. B.Czechoslovakia, Editor.
[15] G.S. Was, Fundamentals of Radiation Materials Science, Springer-Verlag, Berlin, 2007.
[16] L. Tan, J.T. Busby, Formulating the strength factor a for improved predictability of radiation hardening, J. Nucl. Mater. 465 (2015) 724–730, 2015.
[17] S. Queyreau, G. Monnet, B. Devincre, Orowan strengthening and forest hardening superposition examined by dislocation dynamics simulations, Acta Mater. 58 (2010) 5586–5595.
[18] U.F. Kocks, A.S. Argon, M.F. Ashby, Thermodynamics and Kinetics of Slip, Pergamon Press, Oxford, 1975. Progress in Materials Science.
[19] G. Eggeler, N. Nilsvang, B. Ilschner, Microstructural changes in a 12% chromium steel during creep, Mater. Technol. 58 (1987) 97–103.
[20] Y.Z. Shen, et al., TEM investigations of MN nitride phases in a 9% chromium ferritic/martensitic steel with normalization conditions for nuclear reactors, J. Nucl. Mater. 384 (2008) 48–55, 2009.
[21] K. Durst, W. Blum, M. Schwienheer, Coarsening of precipitates and degradation of creep resistance in tempered martensite steels, Mater. Sci. Eng. A 510–511 (2009) 81–87.
[22] X. Xiao, et al., Microstructure stability of V and Ta microalloyed 12%Cr reduced activation ferrite/martensite steel during long-term aging at 650°C, J. Mater. Sci. Technol. 31 (2015) 311–319, 2015.
[23] Q. Huang, Status and improvement of CLAM for nuclear application, Nucl. Fusion 57 (2017) 2017, 086042 (9pp).
[24] R. Kaybyshev, New martensitic steels for fossil power plant: creep resistance, Phys. Met. Metallogr. 109 (2010) 186–200, volumepages2010.
[25] K. Sawada, Creep behavior and stability of MX precipitates at high temperature in 9Cr–0.5Mo–1.8W–VNb steel, Mater. Sci. Eng. A319–321 (2001) 784–787, 2001.